Investigation of feature orientation and consequences of ion tilting during plasma etching with a three-dimensional feature profile simulator

Yiting Zhang[a)]
Lam Research Corp., Fremont, California 94538

Chad Huard[b)]
Department of Electrical Engineering and Computer Science, University of Michigan, 1301 Beal Ave., Ann Arbor, Michigan 48109-2122

Saravanapriyan Sriraman,[c)] Jun Belen,[d)] and Alex Paterson[e)]
Lam Research Corp., Fremont, California 94538

Mark J. Kushner[f)]
Department of Electrical Engineering and Computer Science, University of Michigan, 1301 Beal Ave., Ann Arbor, Michigan 48109-2122

(Received 18 September 2016; accepted 8 November 2016; published 22 November 2016)

Pattern transfer in microelectronics fabrication using plasma-assisted etching processes is being challenged by the three-dimensional (3d) structures of devices such as fin field effect transistors. Etching of 3d structures typically requires a longer over-etch time to clear material in corners, introducing additional selectivity challenges to maintain feature scale critical dimensions. Feature open area, orientation, aspect ratio, and proximity to other nearby structures can influence the outcome of the etch process. In this paper, the authors report on the development and application of a 3d profile simulator, the Monte Carlo feature profile model in the investigation of aspect ratio, and feature orientation dependent etching. In these studies, energy and angularly resolved reactant fluxes were provided by the hybrid plasma equipment model. Results from the model were validated with trends from experimental data. Using reactant fluxes from He/Cl_2 and Ar/Cl_2 inductively coupled plasmas, etching of two dimensional (2d) and 3d structures in the context of ion tilting and orientation of the feature was investigated. © *2016 American Vacuum Society*.
[http://dx.doi.org/10.1116/1.4968392]

I. INTRODUCTION

Plasma etching is an essential step in the fabrication of micro-electro-mechanical-systems and very large scale integrated circuits.[1–3] New transistor structures involving three-dimensional (3d) integration technologies enable the continued miniaturization and performance improvement of electronic systems, but these structures also bring new challenges in fabrication and maintaining critical dimensions (CDs).[4,5] For example, in fin field effect transistor (FinFET) structures, the gate is an extended 3d feature having a large aspect ratio (AR). In order to define the corners at the base and between the gates of FinFETs, an extended over-etch time is required.[6,7] However, this over-etch time may damage the underlying layer. As a result, this process requires high material selectivity to prevent potential damage.[8]

In order to achieve highly anisotropic etching for conductor materials, chlorine (Cl) based plasma chemistries are widely used. Since the spontaneous rate of etching of native Si at room temperature by Cl atoms is relatively low, plasma etching using Cl_2 containing mixtures is driven by ion-induced chemistry.[9] The resulting etch products ($SiCl_n$, $n \leq 4$) typically have a high reactivity and tend to redeposit on the sidewalls of features. This is in general an advantage by preventing undercut of the sidewalls and so enabling fabrication of highly anisotropic features.[10] Other halogen based gas mixtures, such as those containing fluorine (F), are also commonly used in reactive ion etching (RIE) for dielectric materials. However, due to its spontaneous chemical etching mechanism, F-based plasmas usually produce an isotropic etch. With depositing an inhibiting layer on the side-walls of features, anisotropic features can be achieved.[11] For example, dielectric films (e.g., SiO_2) are typically etched using a gas mixture such as $C_4F_8/O_2/Ar$. The fluorocarbon precursors from the plasma produce an inhibiting layer by deposition of a thin polymer. The addition of a small amount of O_2 (≈5%) to the fluorocarbon gas mixture increases the F radical density and promotes F-based etching.[12] The thickness of the polymer film can also be controlled by the oxygen addition, though the SiO_2 is not inert to the oxygen gas. Economou *et al.* reported SiO_2 etch rates up to 0.6 μm/min by oxygen atoms having hundreds of eV of energy.[13] In general, the anisotropic etching of silicon dioxide is mainly ion driven, as ions physically sputter passivation layers and enable F radicals to react with the underlying silicon dioxide.

Although RIE using halogen gases has been extensively investigated, both experimentally and computationally,[14–17] controlling the etch performance of the patterned features

[a)]Electronic mail: Yiting.Zhang@lamresearch.com
[b)]Electronic mail: chuard@umich.edu
[c)]Electronic mail: Saravanapriyan.Sriraman@lamresearch.com
[d)]Electronic mail: Jun.Belen@lamresearch.com
[e)]Electronic mail: Alex.Paterson@lamresearch.com
[f)]Author to whom correspondence should be addressed; electronic mail: mjkush@umich.edu

continues to be a challenge as the CD continues to shrink and ARs continue to increase. Kim *et al.* investigated etching of high aspect ratio contacts in SiO_2 having AR up to 14. Distortion of the contact pattern became significant when the AR increased. Improving the mask material selectivity, increasing the mask thickness, and adding an *in situ* polymer removal step were found to reduce the pattern distortion.[18] Chung investigated aspect ratio dependent etching (ARDE)[19] or RIE-lag of boron-doped p-Si while alternately using SF_6 and C_4F_8 mixtures during Bosch process etching in an inductively coupled plasma (ICP) reactor. He found that trenches having a larger width had higher etching rates. His experimental results with different feature dimensions (2–100 μm) for rectangles, squares, and circles suggested that the dominant factor in RIE lag is the width of the features.[20]

Computational simulations of profile evolution in 3d have provided keen insights into fundamental processes and etch phenomena.[21–26] For example, surface roughening is a major concern in controlling CD. Guo and Sawin investigated the onset of surface roughening using a 3d cellular Monte Carlo simulation and reported that the angle of ion incidence onto the surface was a key parameter for determining the perpendicular and parallel ripples.[21] Tsuda *et al.* developed a 3d Monte Carlo-based simulation to predict the evolution of nanoscale surface roughness for different ion energies and angles.[22] Their model was validated with plasma etching experiments of blanket Si substrates in a Cl_2 plasma. Surface roughening and rippling were found to depend on the angle of ion incidence θ_i. When $\theta_i = 0°$ (normal incidence), concave–convex features were randomly formed on the surface. When θ_i increased to 45° (oblique incidence), ripple structures were formed perpendicularly to the direction of ion incidence. When $\theta_i > 75°$, smaller ripples or grooves were formed parallel to the direction of incidence.

In addition to analyzing surface and line edge roughness, 3d profile simulators have also been developed for optimizing complex processes, such as Bosch deep silicon etching[24] and silicon nitride (SiN) etching.[25] Kuboi *et al.* investigated the time-evolution of plasma-induced damage during SiN etching in hydrofluorocarbon plasmas using a 3d voxel-slab model.[25,26] They demonstrated that the major source of silicon damage in the source/drain region was high energy hydrogen during the over-etch step.

In this paper, results from a computational investigation of 3d feature evolution during etching in an inductively coupled plasma reactor with a Cl_2 based gas mixture are discussed. Although the 3d-model developed for this investigation and described in Sec. II does contain features incorporated into prior 3d models,[21–26] this model was developed with the intent of being as completely general as possible. Although the discussion here is limited to investigations of etching of silicon in Cl_2 containing plasmas, the model is in principle applicable to any etching systems whose processes can be described by a reaction mechanism. The computational model and chlorine etching mechanism were validated with experimental results. The consequences on profile evolution of ion energy and angular distributions (IEADs) and the mask properties are discussed. Features having "U" and "L" shapes were used to investigate over-etch on clearing corners and the consequences of tilting of the ion angular distribution. A description of the computational models used in this investigation is presented in Sec. II. Model validation to experimental trends is discussed in Sec. III. Predicted profiles for investigating CD control in 3d features are discussed in Sec. IV. Conclusions are presented in Sec. V.

II. DESCRIPTION OF THE MODEL

This investigation was conducted by coupling models for the reactor scale and the feature scale. The reactor scale model provided the energy and angular resolved fluxes of neutral and charged species to the substrate. The feature scale model used those fluxes as input to address the evolution of the surface during etching. The reactor scale model employed a surface site balance model to address surface chemistry. However, the coupling between the reactor and feature scale in this investigation was one-way. That is, results from the feature scale model were not cycled back to the reactor scale model.

The hybrid plasma equipment model (HPEM) was used for reactor scale simulation and has been previously discussed in detail in Ref. 27. As a hybrid model, the HPEM has a hierarchical structure in which different modules address different physical phenomena. The main modules used in this study are: the electron magnetic module (EMM), the electron Monte Carlo simulation (eMCS), the fluid kinetics Poisson module (FKPM), and the plasma chemistry Monte Carlo module (PCMCM). The EMM computes the electromagnetic fields generated by the antenna-coils of the inductively coupled plasma investigated here. Those fields are then transferred to the eMCS for calculating electron impact rate coefficients and source functions by a kinetic solution of Boltzmann's equation. The FKPM calculates the densities, fluxes, and energies of the charged and neutral particles. With the densities of charged particles and surface charges, Poisson's equation is solved in the FKPM for the electrostatic potential. When a steady state is reached, the PCMCM is launched to obtain energy and angular distributions of neutrals and charged particles incident onto the substrate.

The Monte Carlo feature profile model (MCFPM) was applied for feature scale simulation. The MCFPM utilizes a rectilinear mesh in two- or three-dimensions having a fine enough resolution to resolve the CD of device. Each cell in the mesh may represent a different solid material or a mixture of materials. The mesh spacing can be adjusted from a nanometer to a micrometer scale. Each mesh cell is assigned a material identity (for example, photoresist, polysilicon, or plasma), which may change during the profile evolution. Solid phase species are represented by the identity of the computational cell; gas phase species are represented by computational pseudoparticles. In the description that follows, the term axial refers to the dimension perpendicular to the plane of the wafer. Lateral refers to the dimensions parallel to the wafer.

In the MCFPM, pseudoparticles are representing radicals and ions and launched toward the surface. Their axial position is several micrometers above the feature while their initial lateral positions are randomly distributed over the extent of the feature. The gas phase species that each pseudoparticle represents is randomly chosen from the total flux of radicals or ions incident onto the substrate produced by the PCMCM. Each particle may represent a fraction of the number of atoms in a solid mesh cell based on the gas-to-material weighting ratio

$$W_g = \frac{1}{\gamma_{gs}} W_s, \tag{1}$$

where W_g is the gas particle weighting, W_s is the surface weighting, and γ_{gs} is the gas-to-surface ratio, which was set to 1 for this study.

The initial velocities of these ions and neutrals are randomly selected from the energy and angular distributions which were generated by the PCMCM. These distributions are flux weighted probability functions $F(\varepsilon, \theta, r)$ which are converted and normalized as cumulative distribution functions $f(\varepsilon, \theta, r)$ by

$$f(\varepsilon, \theta, r) = \frac{\int_0^{\theta} \int_0^{\varepsilon} F(\varepsilon', \theta', r) d\varepsilon' d\theta'}{\int\int F(\varepsilon, \theta, r) d\varepsilon d\theta}, \tag{2}$$

where ε represents energy, θ represents the angle, and r represents the location on the wafer. In practice, different $F(\varepsilon, \theta)$ can be generated by the PCMCM for different locations on the wafer. In this investigation, the $F(\varepsilon, \theta)$ are averaged over the entire wafer.

After initialization, the trajectory of each pseudoparticle is advanced in time in straight lines as charging inside the feature is not considered in this study

$$\vec{v}_i = \vec{v}_{i-1}, \tag{3a}$$

$$\vec{x}_i = \vec{x}_{i-1} + \vec{v}_i \Delta t, \tag{3b}$$

where $\vec{v}$ and $\vec{x}$ represent the velocity and position of the particle where subscripts indicate the former or current time step and Δt is the time-step.

The PCMCM does not record thermal electron fluxes to the substrate. So when addressing charging, electrons fluxes are additionally directed toward the surface with an isotropic angular distribution with velocities randomly selected from a Maxwellian of specified temperature. The magnitude of the flux is determined by having a time-averaged charge-neutral flux to the surface. The top and bottom boundary conditions for potential are set to be Neumann by assuming that the electric field above the feature matches the sheath field and the electric potential below the feature is zero. The left and right boundaries are assumed to follow a periodic Dirichlet condition.

The following describes the lifetime of a particle. At any instant, the time step, Δt, is determined by the time required to move a specified minimum distance. In the absence of charging inside the feature, the trajectory of both neutrals and ions are therefore free-flight. Since the surface is continually evolving, individual particles are usually moved only a fraction of a mesh cell on each time step to avoid inappropriately penetrating below the surface. If the particle intersects with a material cell representing a surface, the particle is moved back to its previous position, the previous time step is halved, and the particle is moved again. This process is iterated until the particle moves within a fraction of the material containing cell, generally no longer than $0.2 \times$ cell width.

While the pseudoparticle is in the plasma, collisions with gas phase particles are allowed during advancement of the trajectory of the particle. A distance between collisions is randomly chosen based on a mean free path, determined by the process operating pressure. All gas phase collisions are assumed to be purely elastic with isotropic scattering and no loss in energy. The final particle velocity after the collision is determined by applying a scattering matrix

$$\begin{aligned} v_x &= v \cdot (\cos\beta \cdot \cos\alpha \cdot \sin\theta \cdot \cos\phi + \cos\beta \cdot \sin\alpha \cdot \cos\theta \\ &\quad - \sin\beta \cdot \sin\theta \cdot \sin\phi), \\ v_y &= v \cdot (\sin\beta \cdot \cos\alpha \cdot \sin\theta \cdot \cos\phi + \sin\beta \cdot \sin\alpha \cdot \cos\theta \\ &\quad + \cos\beta \cdot \sin\theta \cdot \sin\phi), \\ v_z &= v \cdot (-\sin\alpha \cdot \sin\theta \cdot \cos\phi + \cos\alpha \cdot \cos\theta), \end{aligned} \tag{4}$$

where α and β are the polar and azimuthal Euler angles of the velocity prior to the collision; θ and ϕ are the polar and azimuthal scattering angles, and v is the particle velocity before the collision. Due to the low operating pressures during the simulation (tens of mTorr) and the small size of the feature, these gas phase collisions are extremely rare as the particle mean free path is much larger than the simulated feature size.

The initial trajectories chosen from the velocity distributions include nearly isotropic, low energy neutrals, and anisotropic high energy ions. With the exception of charge exchange neutrals that produce sparse neutral particles having tens of eV of energy, the neutral particles generally have energies of <0.1 eV, corresponding to gas temperatures of <1000 K. The main source of energetic particles is ions accelerated through the sheath, which arrive on the wafer with hundreds eV of energy and angular spreads $<10^\circ$ from the vertical. With the assumption that the energetic ions neutralize upon interaction with the surface, nearly equal energetic neutrals can also be produced. As a result, there is no distinguishable difference between surface reactions for energetic ions and energetic neutrals.

In the MCFPM, a generalized mechanism is used in which a reaction for every ion and neutrals species is specified for every solid material species. These processes are input into the model through a list expressed in conventional chemical notation. Probability arrays for the reaction of each plasma species with each surface species are constructed while accounting for the energy dependence of the process. The classes of reactions include adsorption, passivation, deposition, ion activated etching, thermal etching, sputtering, and reflection. All interactions of an ion with the surface neutralize the ion. If the gas phase

particle survives the interaction, the ion leaves the surface as its neutral counterpart. When a pseudoparticle hits a surface cell, a reaction is randomly chosen based on the probability arrays defined by the reaction mechanism.

For those processes having an energy dependence, the reaction probability for a particle of energy E incident onto a surface at an angle θ from the local normal of the surface is[28,29]

$$p(E,\theta) = p_0\left(\frac{E-E_{th}}{E_{ref}-E_{th}}\right)^n f(\theta), \tag{5}$$

where E_{th} is the threshold energy of the process, E_{ref} is a reference energy, p_0 is the probability for a normal incidence (that is $\theta=0$) at E_{ref}, and $f(\theta)$ is the relative probability at the angle of incidence θ. In this work, $n=0.5$, and $f(\theta)$ is an empirical function typical of physical sputtering with a maximum value near $\theta=60°$.[29]

When a particle strikes a surface cell and there is no induced surface reaction or it participates in a surface reaction that generates products in the gas phase, the particle or newly produced particles are emitted into the gas phase. Both specular and diffusive particle reflections are considered. The particles which are desorbed or re-emitted from the surface are generally given thermal speeds and launched with a Lambertian angular distribution with respect to the normal to the surface. When particles strike the surface at large angles with respect to the normal to the surface, specular reflection can occur.[30] To account for surface roughness on spatial scales not resolved by the model, a fraction between the diffusive and specular reflection is specified. The energy of the specular reflected particle is scaled such that the forward scattered particles retain the majority of their incident energy E_i

$$E_s(\theta) = E_i\left(\frac{E_i-E_c}{E_{ts}-E_c}\right)\left(\frac{\theta-\theta_c}{90°-\theta_c}\right), \tag{6}$$

for $\theta>\theta_c, E_c<E_i<E_{ts}$. In Eq. (6), E_{ts} represents the threshold for complete specular reflection, which is set to 100 eV for the cases discussed here. θ_c represents the lower cutoff angle for specular reflection, which is set to 60°. Particles having $\theta<\theta_c$ or $E_i<E_c$ are assumed to diffusively scatter. Particles having $E_i>E_{ts}$ are assumed to retain all of their energy subject to the angular correction. After determining the final reflected particle energy as a sum of both the specular and the diffusive reflected energies, the trajectories of reflected particles or re-emitted products are then tracked in the same manner as an initial injected particle. If a particle trajectory laterally passes outside the computational domain, the particle is reflected back into the domain. If the particle passes out of top of the domain, as though returning to the plasma, the particle is no longer tracked.

The 2d and 3d implementations of the MCFPM are functionally equivalent. The same algorithms are used in both versions, the only difference being resolving the material mesh in the third dimension in the 3d model. Although the algorithms are essentially the same, the computational burden of the 3d version increases from $O(n^2)$ to $O(n^3)$, where n is the average number of mesh cells in a dimension. A typical mesh in 2d, as might be used to simulate a long trench, may be 400×800, whereas in 3d, a typical mesh may be $400\times400\times800$. The added computational burden required more sophisticated numerical techniques as well as parallelization, as described below.

The majority of interactions of particles with surfaces involve a reflection, sputter, or emission of the primary or secondary particle. This in turn requires knowledge of the surface normal. Since the surface is continually evolving, the surface normal is continually changing and so needs to be computed in real time when a particle strikes the surface. Since the mesh consists of cubic blocks, the surface normal is not the actual normal of the face of a computational cell, as that would result in the surface normal only aligned with the coordinate axes. Rather, the surface normal is the vector perpendicular to a plane fitted to the cell centers of a region of the mesh surrounding the point of impact. A dynamic surface advancement algorithm was developed to determine this plane.

When a particle strikes a solid cell, a search is performed of neighboring cells for points that will be used to determine the local plane. This search distance can be small to better represent the high spatial frequency of a rough surface or large to represent low spatial frequencies of a smooth surface (which then performs some intrinsic smoothing). Within the search region, if a neighboring cell has at least one face exposed to the plasma, it is considered a boundary point and its position is recorded. After searching all the cells in the region, those boundary points are used to perform a least squares plane fit to calculate the best fit plane. That is, given a set of points, the coefficients A, B, C, and D are determined, so that the plane $Ax+By+Cz=D$ best fits the boundary points while minimizing the sum of squared errors between the boundary points and the fitted plane.

Given a set of m boundary points P_i with position of (x_i, y_i, z_i), the sum of squared error Q is[31,32]

$$Q = \sum_{i=1}^{m}(Ax_i+By_i+Cz_i-D)^2. \tag{7}$$

Therefore,

$$\begin{aligned}
\frac{dQ}{dA} &= \sum_{i=1}^{m}[2x_i(Ax_i+By_i+Cz_i-D)] = 0,\\
\frac{dQ}{dB} &= \sum_{i=1}^{m}[2y_i(Ax_i+By_i+Cz_i-D)] = 0,\\
\frac{dQ}{dC} &= \sum_{i=1}^{m}[2z_i(Ax_i+By_i+Cz_i-D)] = 0,
\end{aligned} \tag{8}$$

and

$$\begin{aligned}
D &= \frac{\sum_{i=1}^{m}(Ax_i+By_i+Cz_i)}{m} = A\frac{\sum_{i=1}^{m}x_i}{m}+B\frac{\sum_{i=1}^{m}y_i}{m}+C\frac{\sum_{i=1}^{m}z_i}{m}\\
&= A\bar{x}+B\bar{y}+C\bar{z}.
\end{aligned} \tag{9}$$

Combining these expressions produces a set of simultaneous equations

$$\begin{bmatrix} \sum_{i=1}^{m}(x_i-\bar{x})^2 & \sum_{i=1}^{m}(x_i-\bar{x})(y_i-\bar{y}) & \sum_{i=1}^{m}(x_i-\bar{x})(z_i-\bar{z}) \\ \sum_{i=1}^{m}(x_i-\bar{x})(y_i-\bar{y}) & \sum_{i=1}^{m}(y_i-\bar{y})^2 & \sum_{i=1}^{m}(y_i-\bar{y})(z_i-\bar{z}) \\ \sum_{i=1}^{m}(x_i-\bar{x})(z_i-\bar{z}) & \sum_{i=1}^{m}(y_i-\bar{y})(z_i-\bar{z}) & \sum_{i=1}^{m}(z_i-\bar{z})^2 \end{bmatrix} \begin{bmatrix} A \\ B \\ C \end{bmatrix} = \begin{bmatrix} 0 \\ 0 \\ 0 \end{bmatrix}. \tag{10}$$

In order to avoid a trivial solution, the imposed condition on the coefficients is $A^2+B^2+C^2=1$. Equation (10) then becomes an eigenvalue problem which can be solved through use of the Jacobi algorithm. The Jacobi method will return three sets of eigenvectors [A, B, C] representing the best, intermediate, and worst planes. The best plane is recognized by containing the smallest eigenvalue, and its eigenvector is a surface normal vector, which is orthogonal to the best fit plane. The sign of the normal vector is chosen so that the vector points into the plasma (and not into the material).

With the surface normal vector and the particle velocity vector, the direction of the specular reflection is first calculated with respect to the surface normal and then converted back to the Cartesian coordinate system. The conversion is performed by the transformation matrix in Eq. (4), where α and β are the polar and azimuthal Euler angles of the incident velocity, θ is the polar angle of the scatting, ϕ is the azimuthal scattering angles which is randomly chosen in the interval $[0,2\pi]$, and v is the reflected speed of the particle.

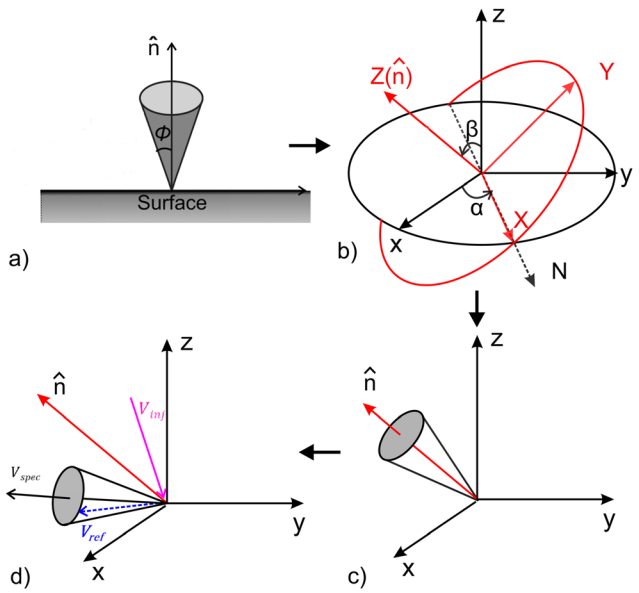

FIG. 1. (Color online) Transformations for scattering angles: (a) The diffusive reflection of a particle will have a Lambertian-like distribution with respect to the surface normal. (b) By having the surface normal as a rotated Z axis from the Cartesian z axis, and having the rotated X axis overlay the intersection of the X-Y and x-y planes, only two Eulerian angles $\boldsymbol{\alpha}$ and $\boldsymbol{\beta}$ are needed. α is the angle between the x-axis and the line of nodes (N axis). β is the angle between the z-axis and rotated new Z-axis. (c) With the Euler angles, the diffusive reflection is calculated back to the master coordinate system. (d) Final particle reflection is a sum of both specular and diffusive reflection.

The diffusive reflection on the surface contains a Lambertian angular distribution with respect to the surface normal as illustrated in Fig. 1(a). This diffusive velocity also needs to be converted in the Cartesian coordinate system and summed with the specular reflection velocity. According to Euler's rotation theorem, rotation of any plane (X, Y, Z) from Cartesian coordinates (x, y, z) may be described using three angles α, β, and γ. The angle α represents a rotation around the z axis, β represents a rotation around the line of nodes (intersection of the x-y and the X-Y coordinate planes), and γ represents a rotation around the Z axis.

In the MCFPM, the surface plane and its normal vector are the new coordinate system, where the surface normal vector is a rotated Z axis from the z axis. The surface plane is a rotation result of the x-y plane, as shown in Fig. 1(b). By assuming the new X axis overlaps on the intersection line (N) of the x-y and the X-Y coordinate planes, the Euler angle γ can be neglected, and the diffusive velocity in the x-y-z coordinate can be converted from:

$$\begin{aligned} &\vec{v}_{dif} = z(\alpha)x(\beta)\vec{V}_{dif}, \quad \text{and} \\ &z(\alpha) = \begin{bmatrix} \cos\alpha & -\sin\alpha & 0 \\ \sin\alpha & \cos\alpha & 0 \\ 0 & 0 & 1 \end{bmatrix}, \\ &x(\beta) = \begin{bmatrix} 1 & 0 & 0 \\ 0 & \cos\beta & -\sin\beta \\ 0 & \sin\beta & \cos\beta \end{bmatrix}. \end{aligned} \tag{11}$$

The final particle reflection velocity is a sum of the diffusive and the specular reflection.

Due to the stochastic nature of the MCFPM, random events can occur which may leave individual or small clusters of cells isolated from the bulk of the etch feature. Such "orphaned" cells or clusters will remain floating in place without mechanical support unless explicitly dealt with by the code. The MCFPM uses two techniques to resolve these orphaned features. The first is to remove these cells from the simulation, as though they represented a small sputtered

particle which would diffuse out of the feature. The second is to vertically drop the isolated cells, as by gravity, onto the underlying surface. To locate orphaned clusters, MCFPM uses the Hoshen–Kopelman cluster labeling algorithm.[33] This algorithm, originally implemented for percolation problems, assigns all cells in the domain a cluster number. All cells which share a side are given the same number, and any two cells which are not directly connected through other solid cells must have different cluster numbers. Once cells are numbered by cluster, MCFPM calculates the size of each cluster. The largest cluster is the main etch feature, and smaller clusters are orphaned cells, which are either dropped or deleted.

The extension of the MCFPM from 2d to 3d increased the effective computational burden by a factor of 100–300 (the dimension of the depth of the mesh), and so, the prior serial implementation was no longer adequate. Making the MCFPM parallel was challenging as the algorithm for advancing the trajectory of any given particle involves a series of logic-trees that involve calls to many subroutines and functions depending on the characteristics of each individual pseudoparticle. In this work, a relatively small number of threads (5–10) was used for advancing the particle trajectories in a parallel implementation. The trajectories of a subset of the particles are run in each thread. Within each thread there are numerous subroutine and function calls to which private variables for that thread are passed. Computationally, this was accomplished by making thread-aware copies of private variables to keep track of the variable during subroutine calls. Copies of the random number generator were also made for each thread to avoid possible collisions during generation of random numbers for separate threads. A small subset of the arrays (such as the material identity of the mesh) is shared between the threads. When elements of these arrays are changed by any individual thread, execution on the other threads is stopped (a critical point) to avoid computational collisions. Since there is a large amount of work associated with the call to each thread, favorable parallel performance (elapsed time compared to serial execution) requires that processors be reserved for each thread to minimize the overhead of redistributing code to the processors.

Since the surface reaction mechanism can be generally considered as an intrinsic property of the gas phase reactant species and the surface species, the reaction mechanism in the MCFPM is independent of process conditions. The process conditions such as the type of plasma source, operation pressures, and gas chemistries may determine the energies and magnitudes of the reactant fluxes to the surface. However, the surface reaction mechanism should be independent of the process conditions.

In this paper, results will be discussed for etching of 3d patterns in silicon using Ar/Cl_2 and He/Cl_2 plasmas. The inert gases in the gas mixture act as a source for energetic ions which deliver activation energy to the surface, but do not otherwise chemically react with the surface. The reaction mechanism used in this investigation for etching of silicon in chlorine containing plasma was adapted from the work of Cheng *et al.*[28] Briefly, the etching of Si with occurs by first chlorinating the surface, forming $SiCl_n$

$$\begin{aligned} &Si(s) + Cl(g) \rightarrow SiCl(s) \\ &SiCl_{n-1}(s) + Cl(g) \rightarrow SiCl_n(s), \quad n < 4. \end{aligned} \tag{12}$$

This surface chlorination is dominantly accomplished by Cl atoms, but can also be achieved by Cl^+ and Cl_2^+. Etching of the passivated polycrystalline, $SiCl_n$, then occurs through subsequent ion activation which generates a volatile product, $SiCl_n$

$$SiCl_n(s) + M^+(g) \rightarrow SiCl_n(g) + M. \tag{13}$$

The energy dependence of these processes is given by Eq. (5).

Mask erosion and redeposition of mask products are important in many processes, particularly in high aspect ratio etching. However, the focus of this investigation is the influence of ion angular distributions on 3d structures. So, all masks except for the experimental validation cases were assumed to be hard-masks (no reaction with any gas species). For the experimental validation of He/Cl_2 plasma etching Si shallow trench isolation (STI), the mask was allowed to erode, as the angular reflection of ions from the mask is important to phenomena such as bowing and necking. The sputter probability of the mask was calibrated to match the experimental results. The reaction mechanism for He/Cl_2 used for silicon etching is listed in Table I.

III. MODEL VALIDATION

A simplified geometry of the etch reactor simulated using the HPEM is shown in Fig. 2(a). The reactor is 52 cm in diameter with a five turn coil on the top of the reactor and was operated at 500 W at 15 MHz. A conductive Si test wafer, 30 cm in diameter, sat in electrical contact with the substrate which was surrounded by a dielectric focus ring. The substrate was powered with a 500 W bias at 15 MHz, and the temperature of the wafer was maintained at 40 °C. The pressure was 10 mTorr with 100 sccm Cl_2 injected from the center nozzles and 50 sccm He injected from a side nozzle. The reaction mechanism for He/Cl_2 used for the reactor scale model is based on Ref. 34. The species in the mechanism are: Cl_2, Cl, Cl_2^+, Cl^+, Cl^-, Cl^*, He, He(2^3S), He(2^1S), He(2^3P), He(2^1P), He(3s), He(3p), He^+, and e. The reaction mechanism includes electron impact excitation and ionization, electron ion recombination, ion–ion neutralization, Penning ionization, and charge exchange.

For the purpose of validating the MCFPM and comparing experimental trends with results from the simulation, an experimental study of He/Cl_2 plasma etching of Si was performed on a research-and-development version of a Lam Research Corp. transformer coupled plasma etch system. In order to observe and understand the mechanistic details of etching, all test cases for validation were conducted with a nonoptimized STI process recipe as the optimized profiles were not expected to show enough variability to fully validate the range of etch behavior observed in the feature scale simulator.

TABLE I. Surface reaction mechanism for Si in He/Cl_2 plasmas.

Species definitions: X gas phase species, X^+ Ion, X* hot neutral. X(s) surface site		
Reaction[a,b,c]	Probability	Footnote
Formation of passivation layer	p_0	
$Cl + Si(s) \rightarrow SiCl(s)$	0.99	
$Cl + SiCl(s) \rightarrow SiCl_2(s)$	0.95	
$Cl + SiCl_2(s) \rightarrow SiCl_3(s)$	0.9	
Formation of etch blocks		
$Cl + SiCl_3(s) \rightarrow SiCl_4$	0.0001	
$Cl^* + SiCl\ (s) \rightarrow SiCl_2$	0.05	d
$Cl^* + SiCl_2(s) \rightarrow SiCl_2 + Cl^*$	0.1	d
$Cl^* + SiCl_3(s) \rightarrow SiCl_3 + Cl^*$	0.42	d
$Cl^+ + SiCl\ (s) \rightarrow SiCl_2$	0.2	d
$Cl^+ + SiCl_2(s) \rightarrow SiCl_2 + Cl^*$	0.4	d
$Cl^+ + SiCl_3(s) \rightarrow SiCl_3 + Cl^*$	0.4	d
$Cl_2^* + SiCl(s) \rightarrow SiCl + Cl_2^*$	0.03	d
$Cl_2^* + SiCl_2(s) \rightarrow SiCl_2 + Cl_2^*$	0.05	d
$Cl_2^* + SiCl_2(s) \rightarrow SiCl_3 + Cl^*$	0.05	d
$Cl_2^* + SiCl_3(s) \rightarrow SiCl_3 + Cl_2^*$	0.15	d
$Cl_2^* + SiCl_3(s) \rightarrow SiCl_4 + Cl^*$	0.15	d
$Cl_2^+ + SiCl\ (s) \rightarrow SiCl_2 + Cl^*$	0.3	d
$Cl_2^+ + SiCl_2(s) \rightarrow SiCl_2 + Cl_2^*$	0.25	d
$Cl_2^+ + SiCl_2(s) \rightarrow SiCl_3 + Cl^*$	0.5	d
$Cl_2^+ + SiCl_3(s) \rightarrow SiCl_3 + Cl_2^*$	0.35	d
$Cl_2^+ + SiCl_3(s) \rightarrow SiCl_4 + Cl^*$	0.35	d
Abstraction from passivation layer		
$Cl + SiCl_2(s) \rightarrow SiCl(s) + Cl_2$	0.01	
$Cl + SiCl_3(s) \rightarrow SiCl_2(s) + Cl_2$	0.03	
Mask resist erosion (R)		
$He^+ + R(s) \rightarrow R + He^*$	0.05	e
$He^* + R(s) \rightarrow R + He^*$	0.05	e
$Cl^+ + R(s) \rightarrow R + Cl^*$	0.045	e
$Cl_2^+ + R(s) \rightarrow R + Cl_2^*$	0.15	e

[a]Unless otherwise specified, all ions neutralize on surfaces, returning as their neutral counterparts.
[b]All gas phase species have units of flux ($cm^{-2}s^{-1}$). All surface species have units of fractional coverage.
[c]In reactions with no chemical change, the gas species are reflected off the surface. These reactions are not shown in the table.
[d]The reaction probability p for incident energy ε is if $\varepsilon_{\text{incident}} > \varepsilon_{th}$ $p = (p_0 \cdot (\varepsilon - \varepsilon_{th})^{0.5})/((\varepsilon_{ref} - \varepsilon_{th})^{0.5}).f(\theta)$, else $p = 0$ where $\varepsilon_{th} = 10\,\text{eV}$, $\varepsilon_{ref} = 100\,\text{eV}$, p_0 is the probability at ε_{ref} and f is a scaling factor for angle of incidence θ.
[e]$\varepsilon_{th} = 15\,\text{eV}$ and $\varepsilon_{ref} = 150\,\text{eV}$.

The predicted plasma density is shown in Fig. 2(b). The peak plasma density is $n_e = 8.6 \times 10^{10}\,\text{cm}^{-3}$, which is sustained by a bulk electron temperature of $T_e = 1.6$–$1.8\,\text{eV}$. The inductively coupled coils provide the majority of power deposition to maintain the plasma density. The substrate bias delivers the majority of its power to the sheath region and contributes to ion acceleration through the sheath. The rf bias amplitude is 500 V, and the dc bias is −379 V. The large dynamic range of ion masses (4–70 amu) produces IEADs that vary from 71–918 eV for He^+ to 268–620 eV for Cl_2^+. The angular spread is <3°. The reactant fluxes to the substrate are Cl_2^+, $9.8 \times 10^{15}\,\text{cm}^{-2}\text{s}^{-1}$; Cl^+, $1.0 \times 10^{15}\,\text{cm}^{-2}\text{s}^{-1}$; Cl, $4.4 \times 10^{17}\,\text{cm}^{-2}\text{s}^{-1}$; and He^+, $6.6 \times 10^{13}\,\text{cm}^{-2}\text{s}^{-1}$. The reactant fluxes and energy-angular distributions were transferred to the MCFPM to provide the initial condition of the pseudoparticles.

Trenches, which are typically used for STI, were chosen to validate 2d etching phenomena. The trenches were experimentally fabricated with a 120 nm (60 nm oxide + 60 nm nitride) thick mask over a silicon substrate. The experimental data came from a line pitch grating structure on the die. Two line/pitch ratios were used, 50/100 and 70/140 nm, to represent dense and semidense features. (A line/pitch ratio of 50/100 means a nominal trench width of 50 nm and a spacing of 100 nm.) Their corresponding end of array trenches was also investigated as being representative of isolated features and are shown on the right side of Fig. 4. The model geometry was in the middle of the array having a width (x dimension) of 100 nm with a trench width of 50 nm, a depth (y dimension) of 40 nm, and a height (z dimension) of 480 nm. The numerical mesh resolution had cubic elements of 0.5 nm on a side. The boundary conditions in the x and y directions were periodic. With these boundary conditions, the small computational region actually represents an infinite length trench with an infinite number of pitches. The simulation region representing the end of an array of

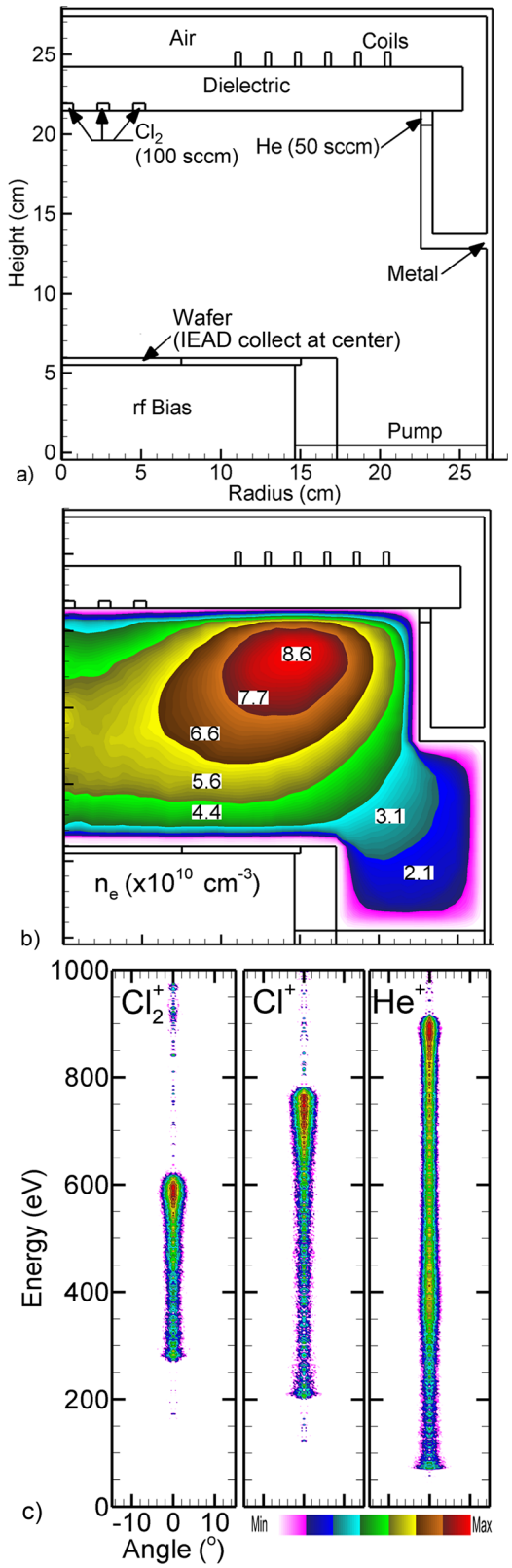

FIG. 2. (Color online) Properties of the inductively coupled plasma. (a) Schematic of the reactor operated at 10 mTorr with 100 sccm Cl_2 injected through center nozzle and 50 sccm He injection through side nozzle. The coils are powered with 500 W at 15 MHz and the electrode is biased with 500 V at 15 MHz. The properties of the He/Cl_2 plasma are (b) time averaged electron density with a maximum of 8.6×10^{10} cm^{-3} and (c) the ion energy angular distributions collected at the wafer center, separately normalized for each species.

trenches has 200 nm of open space on one side (x-dimension) with absorbing boundary conditions with the same dimensions in the x and z directions. The absorbing boundary condition implies when a particle leaves the computational domain, it will be deleted and tracking of its trajectory terminated.

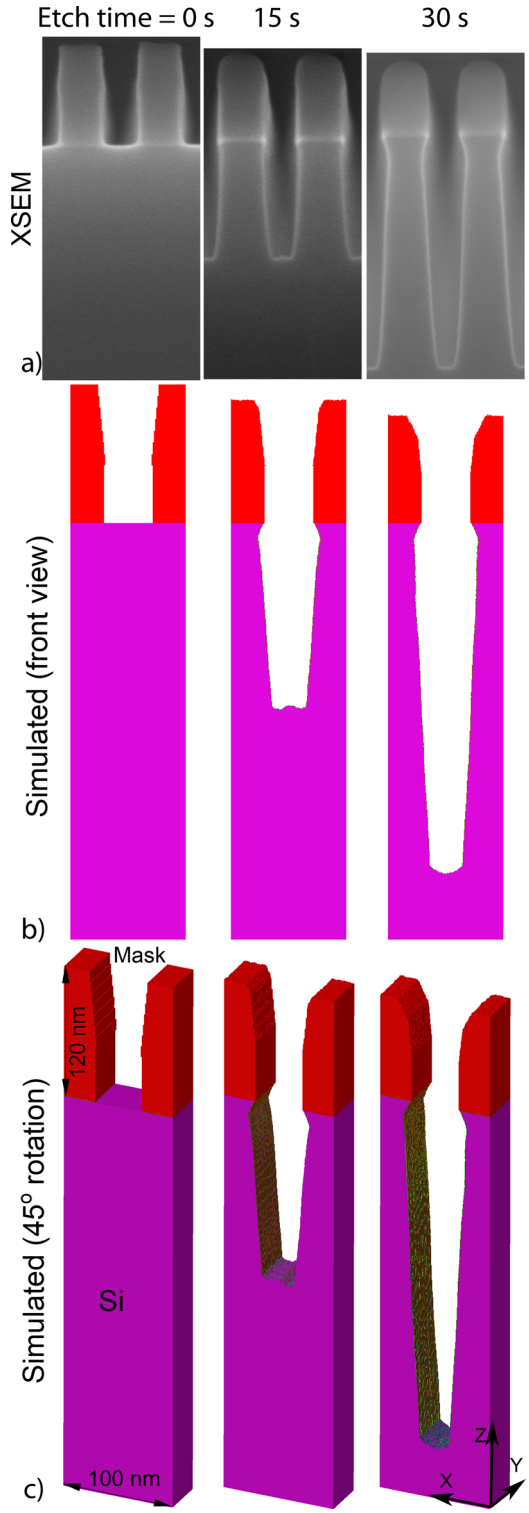

FIG. 3. (Color online) Feature profiles with for a 10 mTorr ICP sustained in a He/Cl_2 mixture for etch times of 0, 15, and 30 s. (a) Experimental SEM, (b) simulated profiles in the x-z plane, and (c) simulated profiles with the z-axis rotated by 45°.

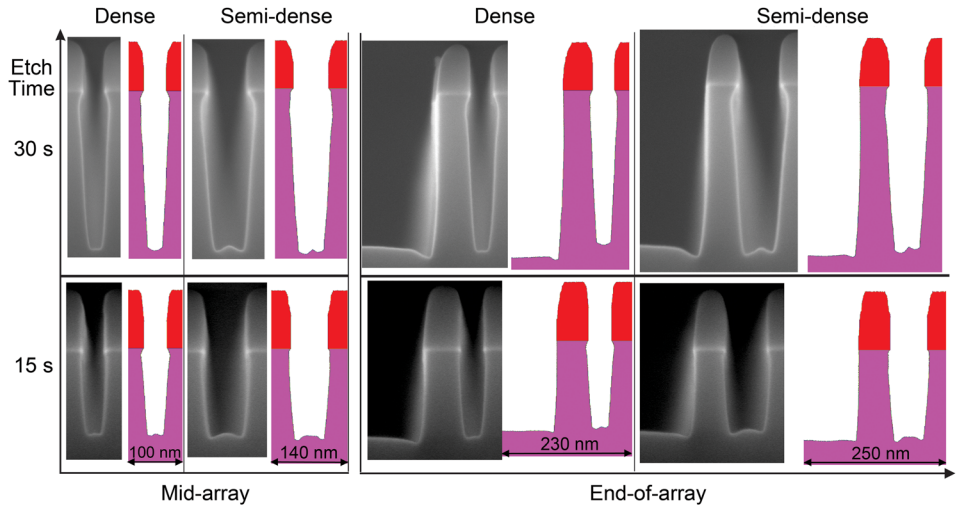

FIG. 4. (Color online) Comparison of simulation and SEM image for features with different open areas at etch times of 15 and 30 s. The operating conditions are 10 mTorr $He/Cl_2 = 50/100$ sccm. The dense trench has line pitch ratio of 50/100 nm and the semidense trench has line pitch ratio of 70/140 nm. The end of array trenches represents isolated features, which have open area of 200 nm. These larger open areas have a higher etch rate. Due to lack of there being reflection from an adjacent mask surface, there is no bowing on the outside of trench in both measurement and simulation.

The experimentally measured and computed profiles for the 50/100 nm dense features are shown in Fig. 3. In these validation cases, the etching time of all experimental and computational results are controlled and kept consistent. As the mask erodes and its height decreases, the top edges of the mask become faceted and rounded. The decrease in height of the mask enables more ion and radical fluxes to reach the mask side wall, which produces a larger facet angle due to the increase in sputter yield with increasing angle. The reduction in mask height also reduces the aspect ratio, and allows ions with progressively larger angles to strike the side walls of the feature, which produces some bowing. The ions reflect off the mask as high energy neutrals to produce the bowing, and off of the sidewalls inside the trench to produce the microtrenches at the bottom of the feature, as shown at 15 s of etching. With a longer etch time (30 s), the bowing of the profile moves downward in the feature as the mask erodes further and the position where hot neutrals reflecting off the mask strike the sidewalls also moves down. With increasing etch time, the two microtrenches merge at the center of the feature and become indistinguishable for the dense trench. Feature bowing is predominantly driven by the ion scattering off the mask. Although chlorine spontaneous etching is included in this study, no significant undercut beneath the mask is observed. These trends are validated by the profile of features at the end of array, which should not have bowing as there is no mask on the other side (open field) to reflect ions.

The four test structures (dense and semidense at middle and end of the array) at two etch times are shown Fig. 4. The model trends match well with the experimental results for all conditions. With larger spacing, the etch rate slightly increases as more reactive flux directly reaches the etch front without reflecting. Unlike the dense feature, the two microtrenches of the semidense features remain separate as the width of the microtrenches is smaller than that of the feature.

The end of array feature shows similar behavior as the middle of array, semidense feature, including microtrenching. However, there is no bowing on the outside wall since there is no nearby mask or sidewall to reflect ions into the wall to produce the bowing. The ion angular distribution is not broad enough to independently produce the bowing. The majority of energetic ions either directly bombard the bottom of the feature, with a small fraction having glancing collisions on the side wall to produce microtrenching. The mask on the open field side of the trench shows asymmetric erosion, as the left side had more ion and radical flux reach that surface compared to that inside of the feature. The influence of the chlorine spontaneous etching can also be evaluated by the outer side of the line in the end-of-array. With 30 s of etching, the outer (left) side of line which faces the open area has a vertical sidewall as shown on the right top corner of Fig. 4. This indicates that only small amount of spontaneous etch occurs during the process. The open area on the left has a faster etch rate in the simulation as it has larger view angle to the plasma. This effect is less severe in the experiments. The discrepancy likely comes from the lack of redeposition of etch products in the open field in the model.

Overall, the predicted characteristics for the 2d features are within 90% of experimental data, as shown in Fig. 5. There is a small difference in the position of the bowing between the experiments and predictions. These differences are likely due to either small differences in the ion angular distributions or due to the need for improvement in the mask erosion and redeposition surface chemistry in the model. Simulation results discussed in Sec. IV show that small changes in the ion angular distribution can produce significant variations in the features.

With the same process conditions as used for the 2d validation, a tip-to-tip feature on the same die was used to validate the 3d prediction capability of the model. The initial mask shape was based on metrology data [top down CD scanning electron microscope (SEM), cross sectional scanning

transmission electron microscopy (STEM)] taken on the three dimensional features, as shown in Fig. 6. The actual mask curvature was simplified in the model as a straight chamfered edge. The actual mask consists of silicon dioxide on top of silicon nitride. As the nitride layer will not be etched within 30 s, the entire mask was assumed to be oxide in the model. The total computational region was $500 \times 180 \times 480$ nm with 1 nm mesh resolution equivalent to 4.32×10^7 cells in total.

The predicted profiles in the x and y directions are compared with STEM images in Fig. 7. The x-cut data show slight bowing and microtrenching as there is a close neighboring surface for refection. The tip-to-tip distance is 238 nm, which is far enough from each other (similar to the open space condition for the end of array trench) that there is no bowing in the y-dimension while showing microtrenching. The corresponding 3d perspectives of the etch feature for times of 7.5–30 s are shown in Fig. 8. [The feature at the initial time is shown in Fig. 6(a).] The passivated poly-Si, $SiCl_x$ (green-yellow color in the plot) is formed on all silicon surfaces exposed to the plasma. Since mixing is not included in this simulation, then passivation (the formation of $SiCl_x$) is limited to a single layer. The passivation is denser on all side walls compared to the bottom of the features as ion bombardment chemically sputters the passivation on the bottom of the feature. The oxide mask shows faceting and rounding at the corners. The 3d results provide more details of the profile evolution than can be observed in the cross-sectional STEM metrology data. For example, microtrenching due to specular reflection of ions form a ditch at the base of the tip whose width grows as the etch proceeds. There is less passivation in the microtrenches as the passivation is eroded due to the higher ion flux. The area between the tips etches slower than the four corners due to the lack of the reflected flux of hot neutrals, which results in an uneven etch front surface after 30 s of etching.

In a brief summary, simulated etch profiles were compared with experimental measurements. In general, a good quantitative agreement was obtained on shape evolution, though the precise positions of bowing in the profile are not captured. This result is likely an outcome of simplifications of the actual shape of the mask and differences in the predicted angular spread of the IEADs for which there are no experimental measurements at this time.

IV. CONSEQUENCES OF REACTANT FLUXES ON 3D STRUCTURES

The influence of IEADs on 3d pattern etching for Si or SiO_2 was computationally investigated using Ar/Cl_2 gas mixtures. The study was performed using the same reactor as previously described and shown in Fig. 2. The plasma was sustained in a 20 mTorr, $Ar/Cl_2 = 80/20$ mixture powered at 800 W (15 MHz) with an rf bias of 100–600 V (15 MHz) on the substrate. The 200 sccm Ar/Cl_2 mixture was injected through the center nozzle. The reaction mechanism for the Ar/Cl_2 plasma used in the HPEM is discussed in Ref. 34. The species in the mechanism are Ar, Ar ($1s_5$, $1s_3$) metastable, Ar ($1s_2$, $1s_4$) radiative, Ar (4p,5d), Ar^+, Cl_2, Cl_2^*,Cl_2^+, Cl, Cl^+, Cl^-, Cl^*, and e. The ion energy distributions (IEDs) of Cl_2^+, Ar^+, and total ions are shown in Fig. 9(a), with the integral of each distribution normalized to 1. The IEDs for each species have a double peak shape. The IED of total ions has a multiple peak distribution due to an overlap of the IEDs of Cl_2^+, Cl^+, and Ar^+. As the flux of Cl_2^+ is 5–7 times larger than the other two ions, the IED of total ions is similar to that of Cl_2^+ with extra minor peaks contributed from the Cl^+ and Ar^+. The surface reaction mechanism for Ar/Cl_2 etching silicon was modified from that for He/Cl_2 in Table I by removing mask erosion.

The bias voltage amplitude was varied from 100 to 600 V, with the resulting IEADs shown in Fig. 9(b). With larger rf biases, the angular distribution of total ions becomes narrower and the energy distribution is significantly extended. The fluxes of the primary reactant species for different biases are in Table II. Although the additional bias power dominantly goes into ion acceleration, a small fraction also contributes to production of reactant species. The

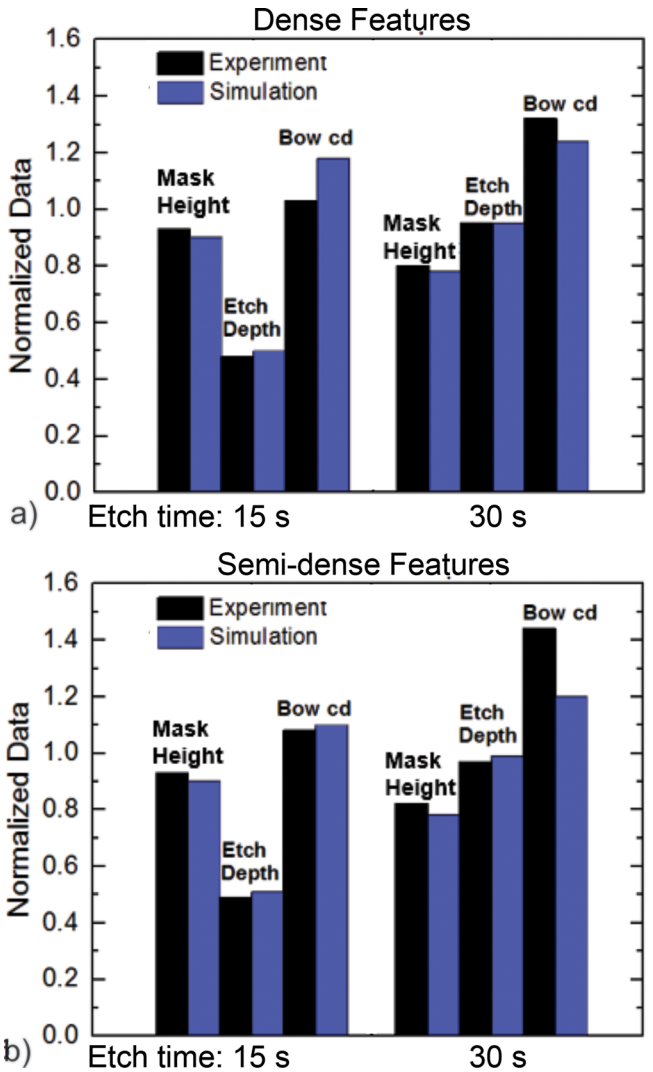

FIG. 5. (Color online) Normalized comparison between simulated profiles and experimental measurements for (a) dense (line pitch = 50/100 nm) and (b) semidense (line pitch = 70/140 nm) features.

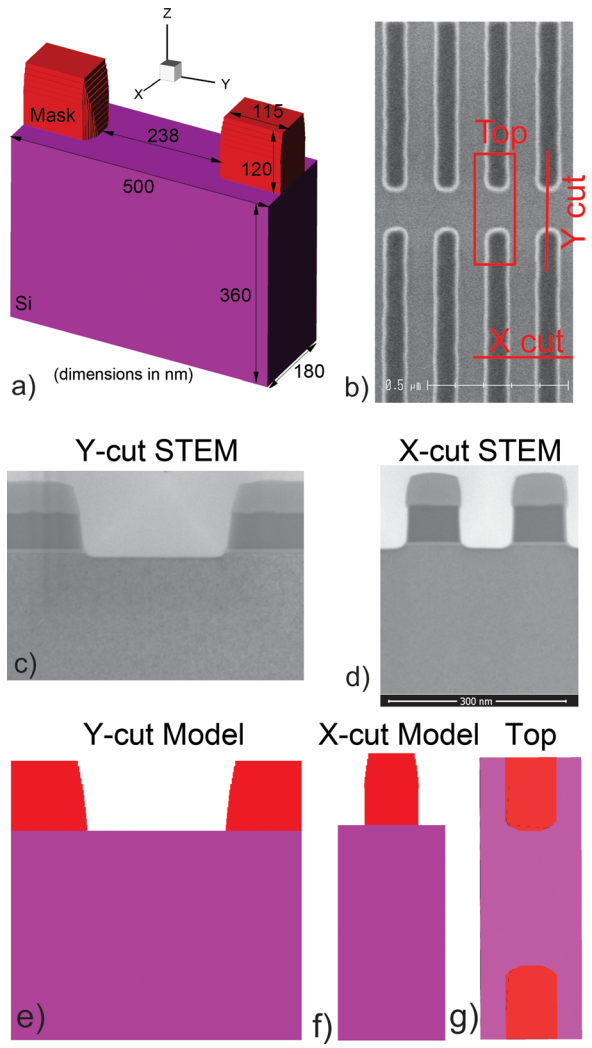

FIG. 6. (Color online) Initial conditions for validation of three-dimensional profile evolution. (a) Tip to tip initial mesh and dimensions for the simulation. STEM imaging showing experimental masking, (b) top view, (c) y-direction, and (d) x-direction. The corresponding model shapes are shown for (e) y-direction, (f) x direction, and (g) top view.

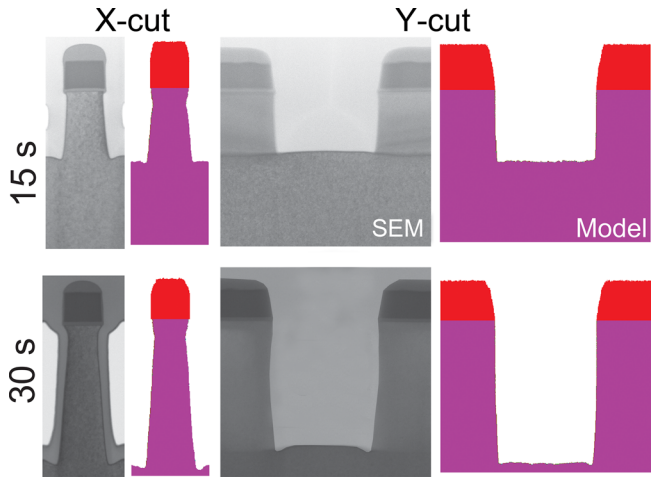

FIG. 7. (Color online) Simulation and experimental (STEM images) of the feature with masking shown in Fig. 6 for etch times of 15 and 30 s. (Left) With small spacing between features, bowing and microtrenching occur in the x-cut. (Right) With large a spacing, only small amount of microtrenching and little bowing occurs in the y-cut.

additional power promotes Cl_2 dissociation in the bulk plasma and produces an increase in the flux of Cl. The ionization potential of Ar (16 eV) is higher than that of Cl (12.99 eV) and Cl_2 (11.47 eV), and so, the Ar^+ flux is smaller than that of the chlorine species.[35] Electron impact ionization is less sensitive to the bias power, and ion fluxes have a small increase with bias power. Since there are no large changes in either neutral or ion fluxes with the change in bias, the dominant variable is the change in angular and energy distributions of the ions.

The impact of different $IEAD_S$ on 3d pattern etching of Si was first investigated with a U-shaped test pattern having a hard-mask (the mask does not react with any incident species), as shown in Fig. 10(a). For these results, the mask is in red, Si appears as blue, the substrate SiO_2 is golden and the green color represents $SiCl_x$ passivation. The selectivity of Si and SiO_2 is assumed to be infinite. The total computational region is $114 \times 210 \times 150$ nm with a mesh resolution of 1 nm (3.6×10^6 cells in total). The width of the legs and top of the U, and of the slot inside the U are 18 nm. Therefore, the aspect ratio is 10 for the middle of the feature between the legs of the mask. Periodic boundary conditions are employed for the front, back, left, and right faces. When a particle passes through the top boundary, it is removed from the simulation.

When the feature is etched with a 100 V bias, 80 s is required to reach the SiO_2 in the open field. The time sequence for the profile evolution is shown in Fig. 10(c). In the beginning of the etching process, t = 20 s, the etch rates inside and outside of the U are similar. As the etching process proceeds, the etch rates begin to differ, with higher rates

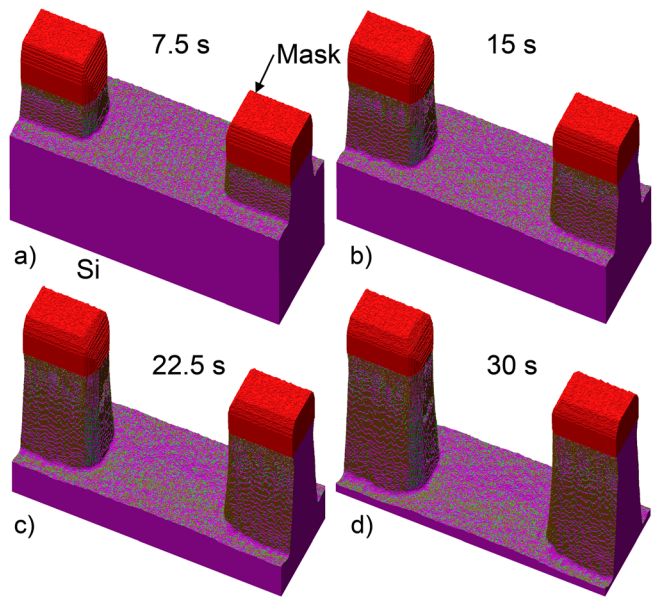

FIG. 8. (Color online) Simulated profiles for plasma etching a tip to tip feature of a Si film (purple) with an oxide mask (red). The yellow regions on the Si are $SiCl_x$ passivation. Results are shown for etch times of (a) 7.5 s, (b) 15 s, (c) 22.5 s, and (d) 30 s. Process conditions are $He/Cl_2 = 50/100$ sccm, 10 mTorr, 500 W coil power at 15 MHz, and 500 V bias at 15 MHz.

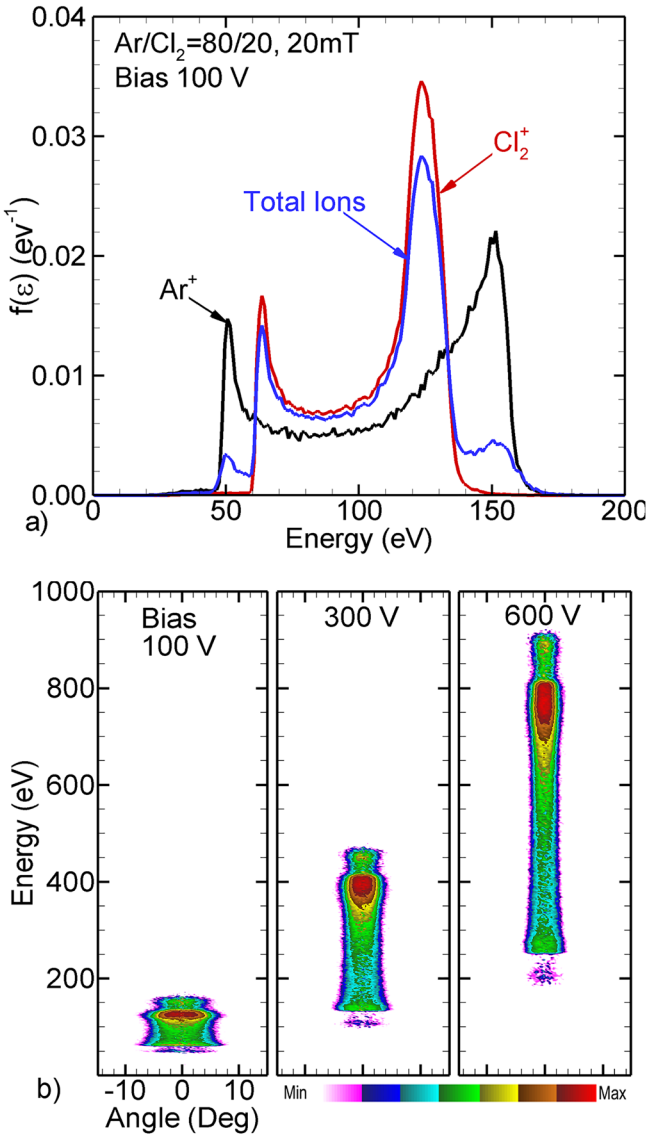

FIG. 9. (Color online) Computed properties of ions for the Ar/Cl_2 plasma. (a) Ion energy distributions for Ar^+, Cl_2^+, and total ions incident onto the wafer for the base case ($Ar/Cl_2 = 80/20$, 20 mTorr, 200 sccm, 800 W coil power at 15 MHz and 100 V substrate bias at 15 MHz). (b) Time averaged ion energy and angular distributions for total ions for substrate biases of 100, 300, and 600 V.

outside the U than inside. With the periodic boundary conditions, the outside open space of the U has a large area exposed to the plasma and a faster etch rate. As the AR inside the U increases with etch depth, the Cl radical flux reaching the etch front inside the U decreases which slows the etch rate. This is an example of ARDE. The decrease in ion-assisted etching forms tapered sidewalls and results in a V-shape etch front inside the U feature, which is then further enhanced due to the angular yield dependence of the chemically enhanced sputtering processes.

In order to completely etch the inside of the U, at least a 25% over-etch is required. The profile for 100 s etch time is shown in Fig. 10(b). The cross sectional views of the features show several deviations from ideal anisotropic features having clean corners. The Si under the mask is undercut due to Cl spontaneous etching. The inner sidewalls of the trench in the middle of the U are bowed due to reflections of energetic particles (shown in the cross-section view of the A cutoff line). Due to the layout of the mask, the Cl radical flux is shadowed and has difficulty in reaching the inside corners of the U. Therefore, the back sidewall inside the feature (shown in cross-section view of the B cutoff line) has a tapered shape (i.e., inability to clear inner corners).

TABLE II. Total fluxes of the reactants onto the wafer vs rf bias voltage.

	Flux ($cm^{-2}s^{-1}$)		
Species	Bias 100 V	Bias 300 V	Bias 600 V
Cl	4.8×10^{17}	5.6×10^{17}	8.0×10^{17}
Cl_2^+	6.7×10^{15}	6.7×10^{15}	6.9×10^{15}
Cl^+	1.2×10^{15}	1.2×10^{15}	1.3×10^{15}
Ar^+	8.9×10^{14}	8.7×10^{14}	8.8×10^{14}

A. Influence of ion energy and angular distribution

The profiles etched with IEADs for 300 and 600 V are shown in Fig. 11. The etch rate for the 600 V bias case is about 35% higher than for the 100 V case, and 29% higher than for the 300 V bias. The profiles with higher energy ion bombardment have less bowing and less undercut, with tapering largely reduced. These improvements are a result of three factors. First, the IEADs for 300 and 600 V biases not only have higher energy but also have narrower angular distributions. These narrower angular distributions effectively reduce the frequency of collisions with the side walls, and those collisions that do occur are more specular. These trends then inhibit bowing. Second, the narrower IEADs having more specular reflection enable more energetic flux to reach the inner corners. Third, since the total etch time and over-etch time are both reduced, the undercut of the mask caused by the Cl spontaneous etching of Si is suppressed. The 600 V bias was selected for investigating the effects of feature orientation and ion angular tilting.

B. Pattern orientation

Ion fluxes to the wafer can have azimuthal and radial asymmetries. Azimuthal asymmetries are fluxes or IEADs that vary as a function of angle around the wafer. Radial asymmetries are variations as a function of radius. A common radial asymmetry to the IEADs is a tilt to the IEAD. As the edge of the wafer is approached, the IEAD will often be tilted in the polar direction. The tilt may be either positive, meaning pointing outward, or negative, meaning pointing inwards. In the following discussion, we investigate the consequences of this radial tilt to the IEAD.

Dies on wafers usually have a rectilinear layout. For example, dies may have a layout with rows parallel to the x direction. In such a layout, the long side wall of the U test structure is parallel to the x-axis. So, the inside trench of the U is parallel, and the back-wall is perpendicular to the radial direction for dies aligned on the x-axis. The inside trench of

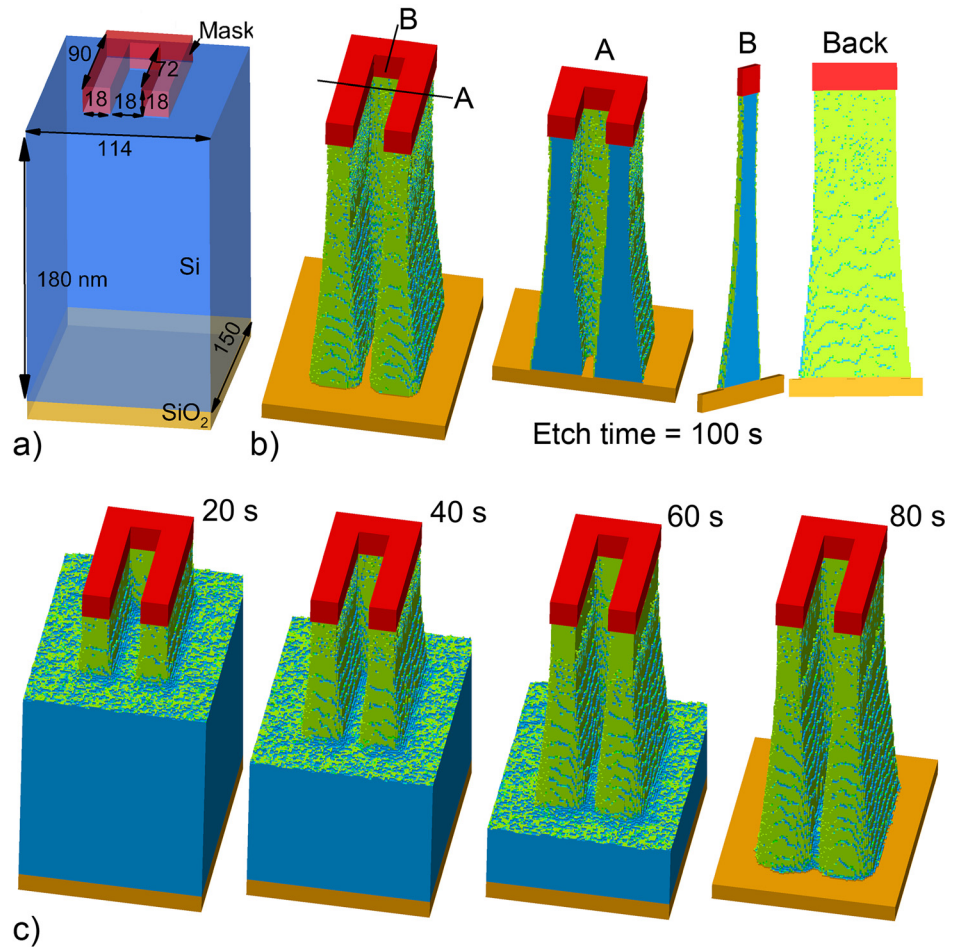

FIG. 10. (Color online) Simulated profile evolution for Ar/Cl_2 plasma etching of the U test structure—Si film (blue) with a hard-mask (red) and SiO_2 substrate (brown)—for the base case conditions ($Ar/Cl_2 = 80/20$, 20 mTorr, 200 sccm, 800 W coil power at 15 MHz and 100 V substrate bias at 15 MHz). (a) Initial profile. (b) Final feature profiles with 100 s etch time. Profiles from left-to-right: Entire feature, middle cross section along the A cutoff line perpendicular to legs of the U, section cut through the back wall along the B cutoff line, and view from the back of the feature. (c) Profile evolution from etch times 20 to 80 s.

the U is perpendicular, and back-wall is parallel to the radial direction for dies aligned on the y-axis.

The origin of etch profiles that depend on the orientation of the feature can be complicated, especially when there are reactive fluxes from the plasma that result in deposition of passivation layers. Not only there is there ion tilting near the edge of the wafer but there may also be orientation dependencies to the deposition fluxes. In this study, our interest was on ion-driven processes, and so, we only considered the role of the angular distribution of ions in investigating the consequences of orientation of the feature. That is, we maintained the isotropic nature of the neutral fluxes and assumed that the ion fluxes were azimuthally symmetric. Only the radial tilt of the IEADs was allowed to change.

In the absence of a tilt to the IEAD (that is, the axis of the IEAD is perpendicular to the wafer), the position of the U on the wafer does not affect the etch characteristics of the structure. For example, the original U shaped mask with the opening aligned with the x-axis was rotated by 90° as shown in Fig. 12. Since particles in the simulation are launched with an azimuthally symmetric angular distribution with the average polar angle being zero, the profile evolution is essentially independent of the orientation of the die. Only a slight difference is observed on the shape of the sidewall due to the randomness of the Monte Carlo simulation.

If we have a positive tilt to the IEAD, the ion flux has a radially outward average angle of incidence. So, considering the test U structure, this means that ion flux pointing radially outward preferentially strikes the outside wall for dies on the x-axis. For dies on the y-axis, an ion flux pointing radially outward is aligned with the center trench, and so, the ion flux preferentially strikes the inside of the feature (or the back-wall if a negative tilt).

To investigate position dependent etching, the ion angular distributions were tilted ±3° along the y-axis, with the results shown in Fig. 13. Results are shown for the original orientation and for the mask rotated by 90°. The arrows show the direction of the tilt in the ion flux. For the original pattern, when ion fluxes are incident slightly inclined towards the left and right in the direction parallel to the y-axis, the two long sidewalls are no longer perpendicular to the substrate at the end of the etch. This effect is best viewed from the back of the feature, or looking directly into the feature. For the original orientation of the U with the ion flux coming from the right [Fig. 13(a)], the sidewall facing the flux is slightly undercut whereas the side wall on the

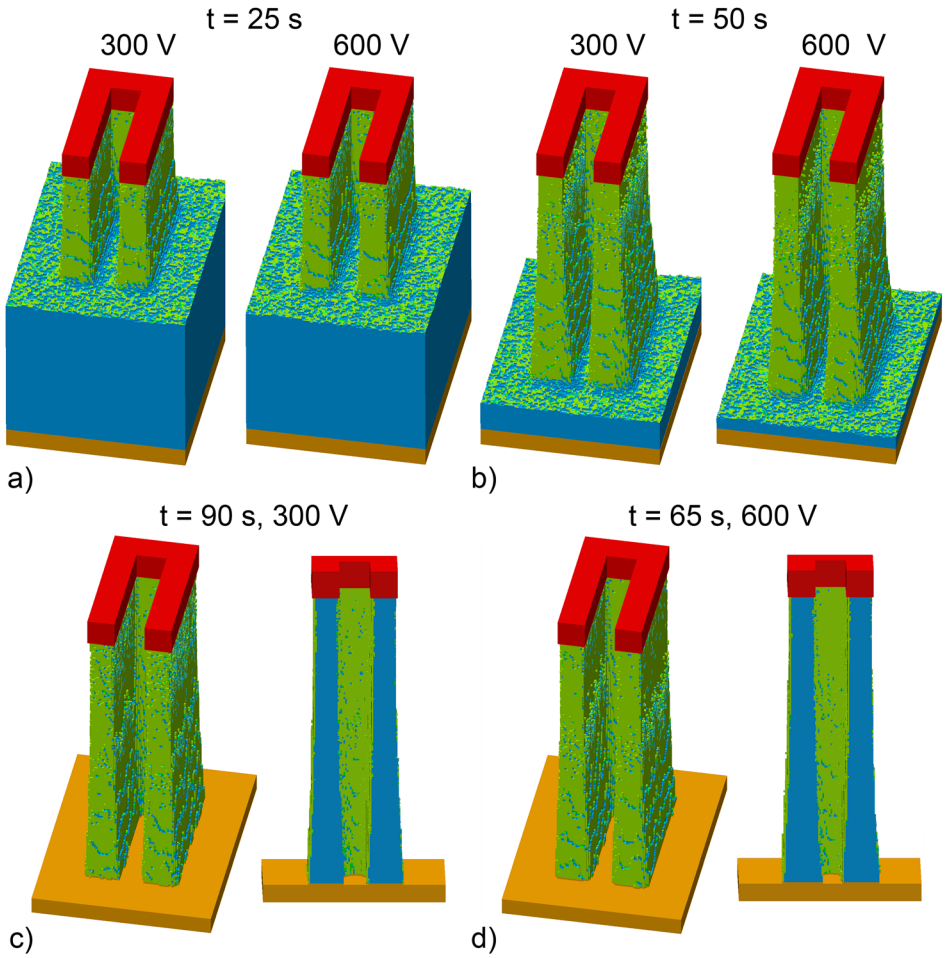

FIG. 11. (Color online) Ar/Cl_2 plasma etching of the U test structure—Si film (blue) with a hard-mask (red) and SiO_2 substrate (brown). Profiles with 300 V bias and 600 V bias at etch times of (a) 25 s and (b) 50 s. Profiles for 20% over-etch for biases of (c) 300 V and (d) 600 V. The cuts are perpendicular to the long legs of the U.

opposite side of the U is sloped outwards. Since this face is downwind of the incoming ion flux, the feature itself produces shadowing of the ion flux that eliminates ions that might be parallel to the face. When the tilt of the ion flux reverses [Fig. 13(b)], the asymmetry of the feature also reverses. When the pattern is rotated by 90° [Figs. 13(c) and 13(d)], the tilt of the ion flux is now parallel to the trench inside the U. When the ion flux is directed toward the back wall [Fig. 13(c)] and the front of the feature is shadowed, the back wall has a slight undercut while the face of the legs of the U are tapered along the direction of tilting. With the tilt of the ion flux reversed [Fig. 13(d)], the face of the legs of the U are slightly undercut while the back wall being leeward of the ion flux is sloped outward.

The slope of the inside walls of the U follow the same general trends as the outside walls. With the original U orientation, the ion fluxes are tilted perpendicular to the long dimension of the trench. The interior trench is then tilted in the direction of the tilt in the ion flux, with there also being significant tapering. The rotated U has the tilt in the ion flux parallel to the axis of the interior trench. There is little angular tilt in the trench. When the tilt in the ion flux strikes the back wall, shadowing of the interior of the trench produces an outward slope to the end of the trench, as shown in Fig. 13(c).

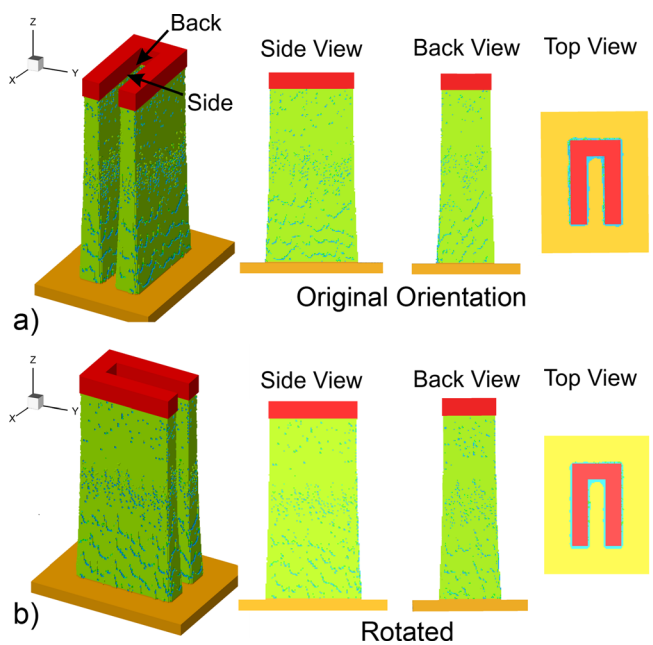

FIG. 12. (Color online) Ar/Cl_2 plasma etching of the U test structure—Si film (blue) with a hard-mask (red) and SiO_2 substrate (brown)—with the 600 V bias. The ion angular distributions are symmetric. (a) Original layout with U aligned with x-axis. (b) Rotated U pattern aligned with y-axis.

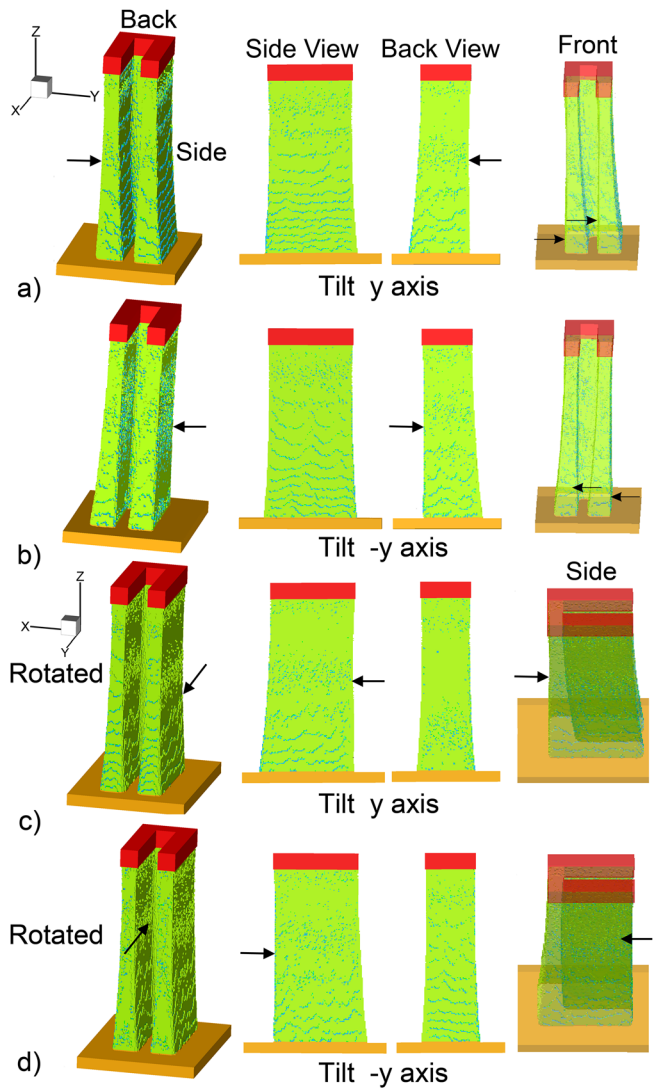

FIG. 13. (Color online) Ar/Cl_2 plasma etching of the U test structure—Si film (blue) with a hard-mask (red) and SiO_2 substrate (brown)—with the 600 V bias and ion angular distributions (IAD) titled by 3° along the y-axis. The direction of the tilt is indicated by the arrows. Original layout with U aligned with x-axis with ion IAD. (a) Tilted by 3° pointing in the positive y-direction and (b) pointing in the –y-direction. Rotated layout U aligned with y-axis with IAD (c) tilted by 3° pointing in the positive y-direction and (b) pointing in the –y-direction.

The shadowing blocks the vertically directed ions that would otherwise produce a vertical etch. When the tilt in the ion flux enters the opening of the trench, the end of the trench has nearly a vertical wall, as shown in Fig. 13(d). The inward tilted ion flux compensates for the narrow view-angle to the plasma of the interior of the trench, a condition that would otherwise produce a sloped sidewall.

These results indicate possible position-dependent asymmetries in features located near the edge of the wafer where ion fluxes often have a radial tilt. Features on dies located on the x-axis have a different orientation to the ion flux than those features on dies located on the y-axis. These two features will have quantitatively different side-wall slopes due to the dot-product of the incident ion flux and the normal to the wall being different.

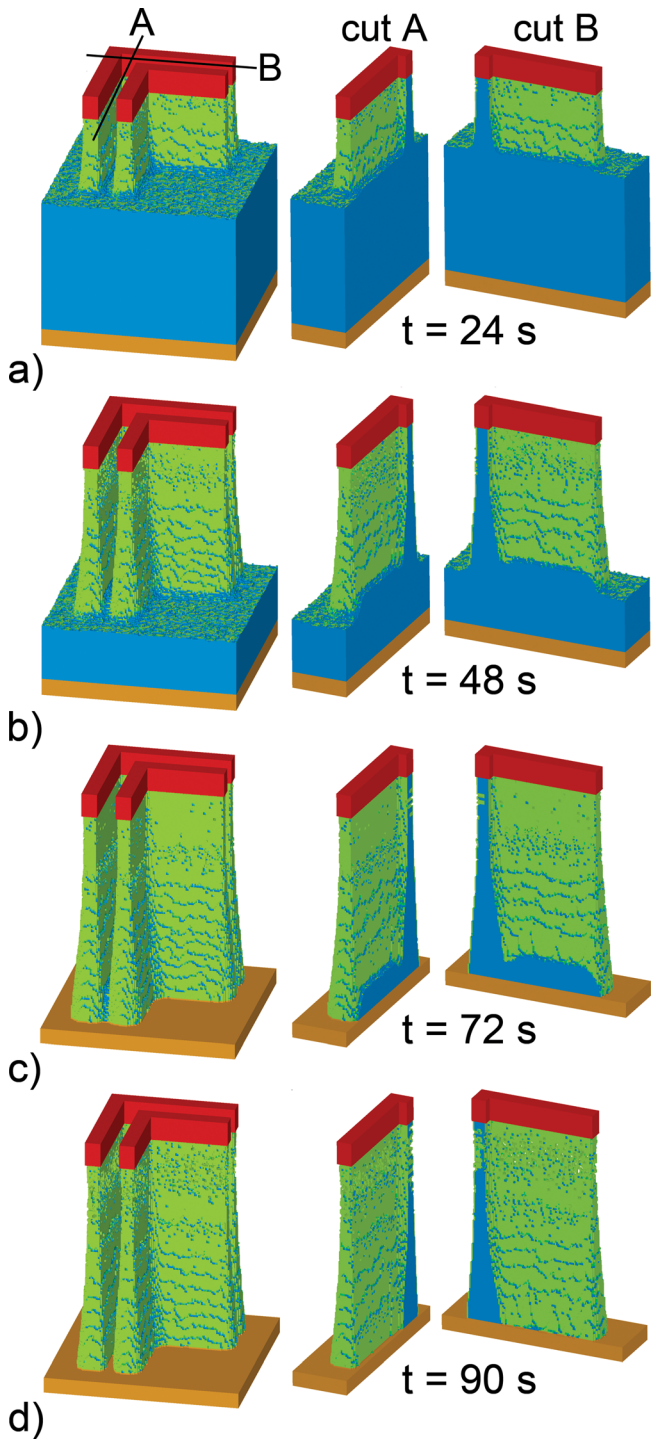

FIG. 14. (Color online) Ar/Cl_2 plasma etching of the L test structure—Si film (blue) with a hard-mask (red) and SiO_2 substrate (brown)—with the 100 V bias at etch times of (a) 24 s, (b) 48 s, (c) 72 s, and (d) 90 s. Cross sections (middle column) in the center of the left trench and (right column) back trench show evidence of aspect ratio dependent etching.

C. Aspect ratio dependent etching within features

The etch rate inside the U displays some features of ARDE. When a feature becomes deeper, the etching species encounter a transport limit to reach the bottom of the feature. With a small view angle to the plasma at the bottom of deep features, the neutrals are shadowed while ions are less

shadowed, an effect that lead to a lower etch rate. In this part of the study, a hard-mask with an L shape trench was used to investigate the ARDE aspects of 3d features. The mask is 18 nm thick, with its longer and shorter sides measuring 90 and 66 nm. The trench has a 12 nm opening and the underlying Si film has a thickness of 150 nm. Therefore, the trench has an aspect ratio of 12.5. The entire computational region is $138 \times 138 \times 180$ nm with 1 nm mesh resolution (3.4×10^6 cells in total). The plasma properties are the same as the U pattern base case having a 600 V bias.

Etching of the L shaped pattern is shown in Fig. 14 as a function of time. Similar to the U pattern case, the etch rate within the trench is smaller than the outside. The aspect ratio of the L shape trench (AR = 12.5) is higher than the U shape (AR = 10), and so, ARDE is more significant in this case. The bottom of the trench along the back (long) leg of the L in Fig. 14(d) is cleared after 25% over-etch while also significantly trimming the side walls. Since the L pattern is diagonally symmetric, the left and back cross sections show similar concave etch front within the trench as shown in the middle (cut A) and right (cut B) columns of Fig. 14. This is also caused by there being a larger plasma view angle at the corner and ends of trenches. The results at 90 s etch time also show that the inner corner is the most difficult to clear since its local AR is the largest and its view-angle to the plasma is the smallest.

V. CONCLUSIONS

The influences of IEADs, feature geometries, and orientation in plasma etching of 3d structures have been investigated using a feature profile model. The profile model addresses reaction mechanisms resulting in etching, sputtering, and deposition on the surface to predict profile evolution based on the fluxes of neutrals and charged particles provided by a reactor scale simulator. The algorithms of the MCFPM were validated by comparing with experimental results of silicon trench and tip to tip etching in He/Cl_2 plasmas.

Etching of 3d structures typically requires long over-etch times to clear corners which then places additional challenges on selectivity to maintain the feature CD. To provide insights to etching of corners in 3d features, etching of U-shaped Si features over SiO_2 was investigated. The resulting profiles suggest that etch profile defects such as bowing and tapering can be overcome through precisely controlling the IEADs. Ions with higher energy and narrower angular distribution are able to clear corners with short over-etch and subsequently reducing the Cl spontaneous etching on the sidewall. When the feature aspect ratio is increased, control of the ion angular distributions becomes important. When the ion flux has a small radial tilt in angle, then etching characteristics become a function of the location of the die or feature on the wafer. Features having sidewalls oriented perpendicular to the ion flux when on the x-axis are parallel to the ion flux when on the y-axis. This leads to position dependent asymmetries.

Aspect ratio dependent etching occurs in many deep silicon etching processes and has many undesired complications in device fabrication. Addressing ARDE is complicated in 3d features since the aspect ratio can change within a feature, an effect that is also exacerbated by the local view angle to the plasma. These aspects of ARDE will be further investigated.

ACKNOWLEDGMENTS

This work was supported by the National Science Foundation (CHE-1004203, PHY-1519117), the Department of Energy Office of Fusion Energy Sciences (DE-SC0001939, DE-SC0014132), and Lam Research Corporation.

[1]H.-D. Ngo *et al.*, J. Phys.: Conf. Ser. **34**, 271 (2006).
[2]S. K. Tolpygo and D. Amparo, J. Phys.: Conf. Ser. **97**, 012227 (2008).
[3]S. F. Yoon, Microelectron. Eng. **14**, 23 (1991).
[4]V. M. Donnelly and A. Kornblit, J. Vac. Sci. Technol., A **31**, 050825 (2013).
[5]M. Puech, J. M. Thevenoud, J. M. Gruffat, N. Launay, N. Arnal, and P. Godinat, "Fabrication of 3D packaging TSV using DRIE," in *Symposium on Design, Test, Integration and Packaging of MEMS/MOEMS 2008* (IEEE, 2008), pp. 109–114.
[6]W. Xu, H. Yin, X. Ma, P. Hong, M. Xu, and L. Meng, Nanoscale Res. Lett. **10**, 249 (2015).
[7]K. J. Kanarik, G. Kamarthy, and R. A. Gottscho, Solid State Technol. **55**, 15 (2012).
[8]A. D. Baily III, M. C. M. van de Sanden, J. A. Gregus, and R. A. Gottscho, J. Vac. Sci. Technol., B **13**, 92 (1995).
[9]W.-C. Tian, J. W. Weigold, and S. W. Pang, J. Vac. Sci. Technol., B **18**, 1890 (2000).
[10]I. W. Rangelow and H. Loschner, J. Vac. Sci. Technol., B **13**, 2394 (1995).
[11]H. Janse, H. Gardeniers, M. de Boer, M. Elwenspoek, and J. Fluitman, J. Micromech. Microeng. **6**, 14 (1996).
[12]R. D'Agostino, F. Cramarossa, S. De Benedictis, and G. Ferraro, J. Appl. Phys. **52**, 1259 (1981).
[13]S. Panda, D. J. Economou, and L. Chen, J. Vac. Sci. Technol., A. **19**, 398 (2001).
[14]J. W. Coburn and H. F. Winters, Appl. Phys. Lett. **55**, 2730 (1989).
[15]S. A. Vitale, H. Chae, and H. H. Sawin, J. Vac. Sci. Technol., A **19**, 2197 (2001).
[16]D. E. Hanson, J. D. Kress, and A. F. Voter, J. Vac. Sci. Technol., A **17**, 1510 (1999).
[17]M. E. Barone and D. B. Graves, J. Appl. Phys. **78**, 6604 (1995).
[18]J. K. Kim, S. H. Lee, S. I. Cho, and G. Y. Yeom, J. Vac. Sci. Technol., A **33**, 021303 (2015).
[19]R. A. Gottscho, C. W. Jurgensen, and D. J. Vitkavage, J. Vac. Sci. Technol., B **10**, 2133 (1992).
[20]C.-K. Chung, J. Micromech. Microeng. **14**, 656 (2004).
[21]W. Guo and H. H. Sawin, J. Phys. D: Appl. Phys. **42**, 194014 (2009).
[22]H. Tsuda, N. Nakazaki, Y. Takao, K. Eriguchi, and K. Ono, J. Vac. Sci. Technol., B **32**, 031212 (2014).
[23]M. Fujinaga and N. Kotani, IEEE Trans. Electron Devices **44**, 226 (1997).
[24]P. Moroz and D. J. Moroz, J. Phys.: Conf. Ser. **550**, 012030 (2014).
[25]N. Kuboi, T. Tatsumi, T. Kinoshita, T. Shigetoshi, M. Fukasawa, J. Komachi, and H. Ansai, J. Vac. Sci. Technol., A **33**, 061308 (2015).
[26]N. Kuboi, M. Fukasawa, and T. Tatsumi, Jpn. J. Appl. Phys., Part 1 **55**, 07LA02 (2016).
[27]M. J. Kushner, J. Phys. D **42**, 194013 (2009).
[28]C. C. Cheng, K. V. Guinn, V. M. Donnelly, and I. P. Herman, J. Vac. Sci. Technol., A **12**, 2630 (1994).
[29]C. F. Abrams and D. B. Graves, J. Appl. Phys. **86**, 2263 (1999).
[30]A. Sankaran and M. J. Kushner, Appl. Phys. Lett. **82**, 1824 (2003).
[31]S. A. Islam, "Math notes—Least squares plane," http://www.sbg.bio.ic.ac.uk/~islam/plane.html.
[32]V. Schomaker, J. Waser, R. E. Marsh, and G. Bergman, Acta Cryst. **12**, 600 (1959).
[33]J. Hoshen and R. Kopelman, Phys. Rev. B **14**, 3438 (1976).
[34]P. Tian and M. J. Kushner, Plasma Sources Sci. Technol. **24**, 034017 (2015).
[35]R. Basner and K. Becker, New J. Phys. **6**, 118 (2004).